Current Tracking Control of Triple Active Bridge DC/DC Converter Under Varying DC-Bus Voltage Conditions

TAKANOBU OHNO ● (Member, IEEE), AND NOBUKAZU HOSHI ● (Senior Member, IEEE)

Department of Electrical Engineering, Tokyo University of Science, Chiba 2788510, Japan

CORRESPONDING AUTHOR: TAKANOBU OHNO (e-mail: takanobu.ohno@ieee.org)

ABSTRACT   A triple active bridge (TAB) converter consisting of three full-bridge inverters and a three-winding transformer has been researched to improve its power conversion performance as a bi-directional isolated multiport converter. Previous research established a current control method using a decoupling system to solve the complex power transmission structure of the TAB converter. However, it is challenging to integrate voltage factors into the decoupling system because DC-bus voltages of the TAB converter are assumed to be constant. Active bridge control against voltage variations has become essential to achieving high-performance DC/DC power conversion systems using high-frequency transformers such as a TAB converter. This paper proposes a TAB converter control method, which is an expansion of the conventional method, to integrate the DC-bus voltage variation into the control model. Model predictive control is used to achieve tracking control by incorporating voltage variation factors into the control method using an established model structure as a basis for predictive calculations. Simulations were conducted to verify that the proposed method improves the output responses compared to the conventional methods when the DC-bus voltages change. Also, experiments using a prototype converter show that the proposed control method can achieve current tracking control during the voltage variation.

INDEX TERMS   Bi-directional power flow, control design, DC-DC power converters, power control.

I. INTRODUCTION

Multiport converter topologies have attracted attention to achieve high efficiency and high-density power transmission in power distribution systems. An energy management system (EMS), which has been spread in recent years, is a system that efficiently operates multiple power sources owned by power consumers, such as photovoltaic cells and storage batteries [1], [2]. Moreover, EMS is expected to develop systems named vehicle to home (V2H) and vehicle to grid (V2G) that utilize automotive batteries for grid operations [3], [4]. While the demand for power converters increases, there are challenges such as efficiency deterioration, conversion cost, and conversion density due to the increase in the conversion stages. Multiport converters, a type of power converter, are being studied because of the ability of power flow control between multiple power sources with a small number of conversion stages [5], [6], [7], [8].

A triple active bridge (TAB) topology shown in Fig. 1(a) is a multiport converter topology with a standard circuit configuration as an isolated bidirectional topology designed by extending a dual active bridge (DAB) topology shown in Fig. 1(b). Inherited from the DAB topology, the TAB converter equips with bi-directional isolated power transmission, soft-switching operation, and wide-range voltage transformation [9], [10]. As shown in Fig. 1(a), the TAB converter consists of three full-bridge inverters as active bridges connected to independent DC-buses, a high-frequency three-winding transformer, and external inductors that adjust the leakage inductances of the transformer.

Due to the converter structure of the TAB converter, a large number of operating modes exist. In principle, the phase difference of the output AC voltages of each full-bridge inverter, called phase-shift, determines the transmission power.
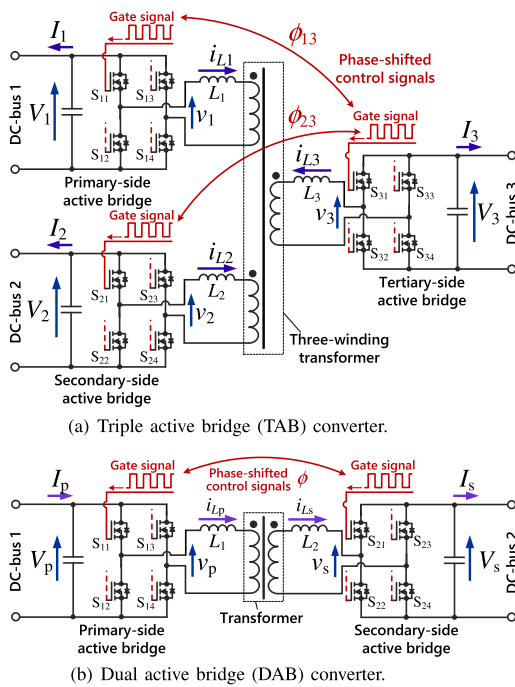
(a) Triple active bridge (TAB) converter.

(b) Dual active bridge (DAB) converter.

FIGURE 1. Circuit configurations of isolated bi-directional DC/DC converters.

Therefore, the converter's operation and power control methods are generally designed around the phase-shift variables.

Because a change in the phase of one active bridge AC voltage affects the phase-shifts of the other two active bridge AC voltages, it is challenging to construct a single input single output control (SISO) model for the TAB converter. In order to solve this problem, the conventional decoupling control method was proposed [11]. In this method, decoupling for the interference is performed by inverse matrix using linearized relationships between phase-shift and fundamental component of output power at steady-state. Power tracking control was achieved by applying proportional-integral (PI) control to this conventional control model [12]. In addition, improvements in the control response using a feed-forward compensator are addressed for a voltage-fed type TAB converter [13], [14]. As for the current-fed type TAB converter, state feedback using the state-space averaging method was applied [15].

As well as maintaining soft-switching conditions, active voltage control are required to suppress the cross-current to the DC-bus voltage variation [16], [17]. Constant power transmission is also required when the TAB converter is applied to a power router application. However, the effects of voltage variation on tracking control performance have not been considered. The voltage variation, which is treated as constant in the decoupling matrix, deteriorates the performance of the current tracking control.

Model predictive control (MPC) is one of the methods used to solve these problems. MPC for the application to power converters has attracted attention for decades due to

its effectiveness for nonlinearity and multi-input multi-output (MIMO) control structure in spite of its high computational cost, high implementation difficulty, and the requirement for convergence of the solution in a short time [18], [19], [20], [21]. Recently, a long-horizon MPC, which has more than one predictive horizon, has successfully been applied to power converters, including modular multilevel converter (MMC) [22], [23], [24]. The long-horizon MPC is also practical for the TAB converter because the control systems for MMC and TAB are similar in that both control systems have MIMO and nonlinearity characteristics. However, the challenge is that the standard MPC quadratic programming (QP) solver cannot be used for the control system of the TAB converter because of the state-space equation structure, including explicitly nonlinear expressions. In contrast, the standard QP solver can be applied to the control system of the MMC by using a linear or bilinear model [25].

This paper proposes a control method that considers the voltage variation to solve these problems. The proposed method is an extension of the conventional decoupling control method. The proposed method mainly consists of feed-forward control to derive the following control input from measured current and voltage values, assisted by simple feedback control to compensate for disturbances. The feed-forward control part is implemented as a model-based prediction controller represented by a discrete first-order delay system based on a steady-state power transmission operation of the TAB converter established in previous research [11], [12]. Error compensation systems, including output feedback, accompany the feed-forward control part. C/GMRES, a nonlinear fast algorithm, is adapted as an algorithm to solve the optimization problem of MPC to satisfy the requirement of the TAB converter control system. An additional integrator structures an expanded system to achieve servo control for current tracking.

This paper is organized as follows: the following section describes the principle of C/GMRES algorithm and modeling of the TAB converter; followed by simulation verification for performance comparison in Section III; Section IV describes the implementation and the experimental results; and at last, Section V is the conclusion.

II. CONTROL MODEL OF TAB CONVERTER FOR C/GMRES METHOD
This section introduces general numeric model predictive control formulation and C/GMRES algorithm. In addition, the steady-state transmission power model of the TAB converter is described. Finally, the proposed control model is explained in detail.

A. C/GMRES ALGORITHM [26]
The discretized predictive responses $x_u(k)$, a function of time t and control input u, are expressed as

$$x_u(0) := x(0) = x(t) \tag{1}$$

$$x_u(k+1) = f(x_u(k), u(k)) \ (k = 0, \ldots, N-1), \tag{2}$$

where $x_u \in X = \mathbb{R}^n$ represents the state variables, $u(k) \in \mathbb{R}^m$ represents the input variables at discrete-time k, f represents state equation, and N represents the term of prediction called horizon. The index u of the state variables means that control input u changes the predicted response of the state variables x. In MPC, the optimal control input u^* is obtained for the initial state $x_{(0)}$ in each control cycle at time t by minimizing the following evaluation function J as

$$J = \varphi(x(N)) + \sum_{k=0}^{N-1} L(x(k), u(k), k), \qquad (3)$$

where the scalar function φ represents the terminal cost, and the scalar function L represents the stage cost called Lagrangian. Both functions are artificially designed for optimality. In other words, MPC is the control law that determines optimal input u^* using state variables $x(t)$ and evaluation function as

$$u^*(t) = \mu(x(t)), \qquad (4)$$

where μ represents the control law. The C/GMRES method derives the optimal solution from necessary and sufficient conditions under the assumption that the form of the evaluation function is a quadratic form. The necessary and sufficient conditions are represented known as Euler-Lagrange as

$$x(k+1) = f(x(k), u(k), k) \qquad (5)$$

$$\lambda(k) = H_x(x(k), u(k), \lambda(k+1), k)^{\mathrm{T}} \qquad (6)$$

$$\lambda(N) = \varphi_x(x(N))^{\mathrm{T}} \qquad (7)$$

$$H_u(x(k), u(k), \lambda(k+1), k) = 0, \qquad (8)$$

where H_x, φ_u, H_u represents partial derivative of scalar functions H, φ by x, u. $H(x, u, \lambda, k)$ represents scalar function expressed as

$$H(x, u, \lambda, k) = L(x, u, k) + \lambda^{\mathrm{T}} f(x, u, k), \qquad (9)$$

where $\lambda(k) \in \mathbb{R}^n$ represents a Lagrange multiplier called adjoint variable corresponding to the state variable $x(k)$.

The algorithm to calculate the optimal solution u^* is the following. First, (5)~(7) are calculated sequentially to obtain the state variables $x_u(k)$ and adjoint variables $\lambda(k)$ using certain input u. Second, calculate the variation of control input Δu, which minimizes error matrix F, defined as the following equation.

$$F(U(t), x(t), t) := \begin{bmatrix} H_u^{\mathrm{T}}(x_{(0)}(t), \lambda_{(1)}(t), u_{(0)}(t)) \\ H_u^{\mathrm{T}}(x_{(1)}(t), \lambda_{(2)}(t), u_{(1)}(t)) \\ \vdots \\ H_u^{\mathrm{T}}(x_{(N-1)}(t), \lambda_{(N)}(t), u_{(N-1)}(t)) \end{bmatrix}$$
$$(10)$$

The vector $U(t) \in \mathbb{R}^{mn}$ is defined as the sequence of the input vectors as

$$U(\tau) = \left[u_{(0)}^{\mathrm{T}}(\tau)\, u_{(1)}^{\mathrm{T}}(\tau) \cdots u_{(N-1)}^{\mathrm{T}}(\tau) \right]^{\mathrm{T}}, \qquad (11)$$
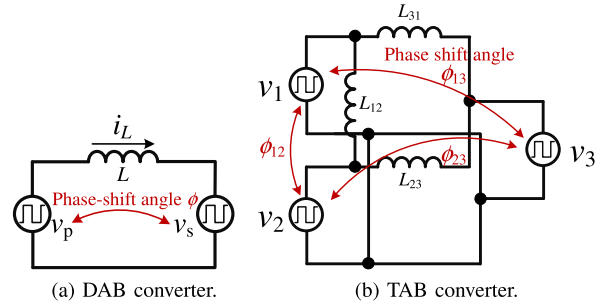

(a) DAB converter. (b) TAB converter.

FIGURE 2. AC-side equivalent circuit of DAB and TAB converter.

where τ represents the continuous-time variable used for calculations inside the controller. The following differential equation is numerically solved to minimize F.

$$\frac{d}{d\tau} F(U(\tau), x(\tau), \tau) = -\zeta F(U(\tau), x(\tau), \tau) \quad (\zeta > 0) \quad (12)$$

For a solution $U(0)$ satisfying the initial condition $F(U(0), x(0), 0) = 0$, error matrix F is maintained at 0 by the control input vector U, which is derived from integrating the solution expressed as the following equation.

$$\Delta U := \frac{dU}{d\tau} \Delta \tau \qquad (13)$$

$$U(\tau + \Delta \tau) = U(\tau) + \Delta U \qquad (14)$$

If $U(0)$ does not satisfy $F(U(0), x(0), 0) = 0$ caused by calculation error, F converges exponentially to 0 due to the effect of the ζ term in (12). At each continuous time τ, (12) is considered as a numerical linear equation for $dU/d\tau$, and generalized minimum residual method (GMRES) is applied as the solution algorithm. In addition, the change of the optimal inputs ΔU at each update period $\Delta \tau$ [s] is traced.

Finally, when the state variables change at the next sampling period, the command value is updated with $u_0(\tau)$, and the calculations (5)~(12) are repeated with the initial condition $U(t)$. Since this method is a continuation method, the values at the end of the update period $U(t + \Delta t)$ are saved and used as the initial value $U(t)$ for the next update period.

B. STEADY-STATE POWER TRANSMISSION MODEL

The steady-state operation model of the TAB converter is derived based on the operation model of the DAB converter. The AC-side equivalent circuit of the DAB converter, which dominantly determines the transmission power, is shown in Fig. 2(a). Where v_p and v_s [V] represent square waveform output voltages of each full-bridge inverter, L_{dab} [H] represents the sum of leakage inductance of the transformer and the external inductor, and ϕ [rad] represents the phase-shift between v_p and v_s. According to the equivalent circuit, the transmission power of DAB converter P_{DAB} [W] is expressed as

$$P_{DAB} = \begin{cases} \dfrac{V_p V_s}{2\pi f_{sw} L_{dab}} \phi \left(1 - \dfrac{\phi}{\pi}\right) & (\phi \geq 0) \\[3mm] \dfrac{V_p V_s}{2\pi f_{sw} L_{dab}} \phi \left(1 + \dfrac{\phi}{\pi}\right) & (\phi < 0), \end{cases} \qquad (15)$$
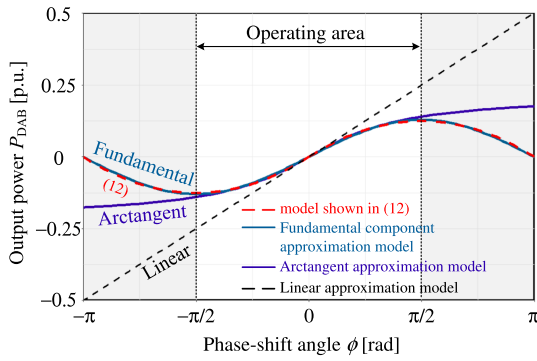
FIGURE 3. Comparison of power transmission approximation of DAB converter.

FIGURE 4. Block diagram of the proposed control system for TAB converter with C/GMRES algorithm. (The system as control object of the algorithm is expanded with an integrator, sensors, and filters.)

where V_p and V_s [V] represent DC-bus voltages corresponding to v_p and v_s, respectively; f_{sw} [Hz] represents the switching frequency. As described later in Section IV, model prediction processes require high-speed calculation with a partial derivative of the power transmission model in NMPC. In addition, the calculation procedures are implemented by logic circuits in FPGA for fast calculations. Thus, the power transmission model with a simple derivative representation, which can be implemented by logic circuits, is desirable. To satisfy this requirement, this paper uses an arctangent approximation model expressed as

$$P_{DAB} = \frac{\gamma 4 V_p V_s}{\pi^3 f_{sw} L} \arctan \phi, \qquad (16)$$

where γ represents the approximation coefficient to make fine adjustments of the function. In this paper, γ is set to 1.08 based on the least square error condition for (15).

Fig. 3 shows a comparison of the transmission power models normalized by $V_p V_s / (f_{sw} L_{dab})$. In addition to (15) and (16), the commonly used linear and fundamental wave approximation models are also shown in Fig. 3. The figure shows that the arctangent approximation model (16) adequately approximates (15) in the operating area.

This modeling part remains to be discussed for the following reasons. Approximation and its error in modeling affect the necessity for error compensation systems. Table modeling instead of functions is possible as another modeling approach. In this paper, the modeling is based on a simple configuration: an approximate model and an output compensation system, which is easy to implement.

The AC-side equivalent circuit of the TAB converter is obtained by applying the Y-Δ transformation to the three-winding transformer, as shown in Fig. 2(b). Where $v_1 \sim v_3$ [V] represent the output voltages of each full-bridge inverter, L_{12}, L_{23}, and L_{31} [H] represent equivalent inductances derived by Y-Δ transformation of leakage inductance, and ϕ_{12}, ϕ_{23}, ϕ_{13} [rad] represent phase-shift amount between output voltages corresponding to the index numbers. As Fig. 2(b) shows, the circuit structure between two power sources equals
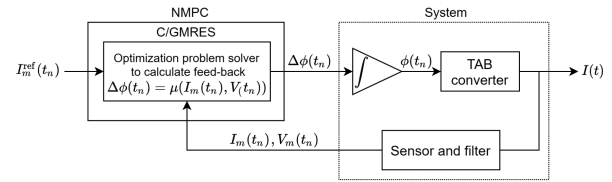
the equivalent circuit of the DAB converter. Thus, the transmission powers of the TAB converter are described as

$$P_1 = - P_2 - P_3 \qquad (17)$$

$$P_2 = \frac{\gamma 4 V_2}{\pi^3 f_{sw} 3 L} \left(V_1 \tan^{-1} \phi_{12} + V_3 \tan^{-1}(-\phi_{23}) \right) \qquad (18)$$

$$P_3 = \frac{\gamma 4 V_3}{\pi^3 f_{sw} 3 L} \left(V_1 \tan^{-1} \phi_{13} + V_2 \tan^{-1}(\phi_{23}) \right), \qquad (19)$$

where $P_1 \sim P_3$ [W] represent the transmission power received by each power source $v_1 \sim v_3$. Also, $V_1 \sim V_3$ [V] represent DC-bus voltages corresponding to $v_1 \sim v_3$, and L represents equivalent inductance under the assumption that all equivalent inductors L_{12}, L_{23}, and L_{31} have the same value to simplify the representation of the model.

C. MODELING OF THE PROPOSED CONTROL

In this chapter, the control model of the TAB converter is derived based on Section II-A and II-B. Fig. 4 shows an overview of the entire proposed control system. Since C/GMRES is a stabilization algorithm, an expanded system including an integrator is necessary to achieve tracking control [27]. Note that C/GMRES algorithm optimizes not ϕ itself but $\Delta\phi$ because the stabilization algorithm behaves as a regulator. An expanded system with an integrator is necessary to form a servo system, which is required as a control system for the TAB converter. Also, the expanded system includes measuring systems such as sensors, A/D converters, and low-pass filters. Index characters n, m, and k represent the following meanings.

- Index $n \in \mathbb{N}$: sample-and-hold number in the main control loop subjected to actual time t [s].
- Index m: state variables with index m represent measured and calculated values that are only treated in the controller distinguished from actual parameters.
- Index $k \in \{0, 1, \ldots, N\}$: discretized prediction time step from 0 to horizon N subjected to prediction time τ [s] in the controller.

It is assumed that the variations of the DC-bus voltages are sufficiently slow compared to the variation of the DC-bus currents. This assumption is reasonable because the operating frequency of the converter is in the order of microseconds, while the voltage variation speed of DC power supplies such as solar cells and lithium-ion batteries is in the order of

seconds. When sensing, filtering, and response delays are expressed as a first-order delay system, the state equation of the current at each sampling period is derived according to (18) and (19) as

$$I_{2m}(k+1) = \alpha I_{2m}(k) + P_a\{V_{1m}(k)\arctan\phi_{12}(k)$$
$$+ V_{3m}(k)\arctan(\phi_{12}(k) - \phi_{13}(k))\} \quad (20)$$

$$I_{3m}(k+1) = \alpha i_{3m}(k) + P_a\{V_{1m}(k)\arctan\phi_{13}(k)$$
$$+ V_{2m}(k)\arctan(\phi_{13}(k) - \phi_{12}(k))\}, \quad (21)$$

where α represents the coefficient of the first-order delay, and P_a is the active power coefficient defined as $P_a := 4\gamma/(\pi^3 f_{sw} 3 L)$ from (18) and (19). (20) and (21) can be summarized as

$$I_m(k+1) = f(I_m(k), \phi(k-1) + \Delta\phi(k), V_m(k), k), \quad (22)$$

where the vector variables are defined as

$$I_m(k) = [I_{2m}(k), I_{3m}(k)]^T$$
$$\phi(k) = [\phi_{12}(k), \phi_{13}(k)]^T$$
$$V_m(k) = [V_{1m}(k), V_{2m}(k), V_{3m}]^T$$
$$\Delta\phi(k) = [\Delta\phi_{12}(k), \Delta\phi_{13}(k)]^T. \quad (23)$$

(22) represents the state equation of the C/GMRES control system with $I_m(k)$ as the state variable and with $\Delta\phi(k)$ as the control input. In addition, the current reference trajectory $I_m^{ref}(k) = [I_{2m}^{ref}(k), I_{3m}^{ref}(k)]^T$ is defined as the ideal first-order response as

$$I_m^{ref}(k+1) = \alpha I_m^{ref}(k) + (1-\alpha)I_{com}, \quad (24)$$

where $I_{com} = [I_{2com}, I_{3com}]^T$ represents the command values of the currents.

Since the C/GMRES algorithm does not have an output feedback mechanism, output offsets due to disturbance and modeling errors occur. To solve this problem, a method to compensate for the offset by changing the command values and state variables in C/GMRES calculations was proposed [28], [29]. A previous study proposed exponential compensation for systems with a large time constant. In this paper, since the time constant of the system is very short, stepwise compensation is used as defined by the following equations.

$$I_{com\_offset(k)} = \begin{cases} I_{com} - I_{m(k)} & (|I_{com} - I_{m(k)}| \le I_{com\_vic}) \\ 0 & (\text{otherwise}) \end{cases}$$

$$I_{offset(k)} = \begin{cases} I_{m(1)} - I_{m(k)} & (|I_{m(1)} - I_{m(k)}| \le I_{vic}) \\ 0 & (\text{otherwise}) \end{cases}$$

$$(25)$$

$I_{m(1)}$ represents the first element of predicted current $I_{m(k)}$ calculated by the state equation calculator at each input update period. Also, I_{com_vic}, I_{vic} represents design variables that determine the boundary where the compensation is conducted.

The terminal cost φ and the stage cost L are designed with the general quadratic equation as

$$\varphi(I_{m(N)}) = \frac{1}{2}(I_{m(N)} - I_{com})^T R(I_{m(N)} - I_{com})$$
$$(26)$$

$$L(I_{m(k)}, \Delta\phi_{(k)}, k) = \frac{1}{2}(I_{m(k)} - I_{m(k)}^{ref})^T Q(I_{m(k)} - I_{m(k)}^{ref})$$
$$+ \frac{1}{2}\Delta\phi_{(k)}^T W \Delta\phi_{(k)}, \quad (27)$$

where $R = \text{diag}[r, r]$, $Q = \text{diag}[q, q]$, $W = \text{diag}[w, w]$, and r, q, w are the design parameters to determine the operation.

Summarizing the above, Fig. 5 shows the block diagram of the entire proposed control system in detail. First, the reference trajectory I_m^{ref} is calculated by the current reference generator using command value I_{com} and sensing parameters $I_m(t_n)$. Second, state and adjoint equation calculators calculate state variables $I_{m(k)}(\tau) = [I_{m(0)}(\tau), \ldots, I_{m(N)}(\tau)]$ and adjoint variables $\lambda_{(k)}(\tau) = [\lambda_{(1)}(\tau), \ldots, \lambda_{(N)}(\tau)]$ using initialized control input vector $\Delta\phi_{horizon}(0)$, the reference trajectory $I_{ref\_horizon}$, and measured parameters $I_{m(0)} = I_m(t_n)$ and $V_{m(0)} = V_m(t_n)$. The control input tracking calculator calculates the change of the control input $\Delta\phi_{horizon}(\tau)$ that satisfies the optimal conditions as far as possible in each input update period by solving (12). Finally, at the next sample-and-hold timing t_{n+1}, the control inputs are updated by the initial term of the control input vector $\Delta\phi_{(0)}$.

III. SIMULATIONS

In this section, the simulation results of the application of the control method are discussed. Section III-A describes the details behavior of the circuit operation applied with the method described in Section II. The design of each control parameter and the effect of the parameters on the circuit operations are verified. The following Section III-B verifies the validity of the control method by comparing the control methods when the DC-bus voltage changes.

A. PARAMETER DESIGN OF C/GMRES
Table 1 shows the basic parameter sets of the proposed control system. Control horizon N and update time of input vector Δt [s] strongly depend on the hardware configuration and implementation of the actual controller. In other words, N and Δt are determined by the limit of the controller resources. Also, Δt, which includes the GMRES iteration calculations, determines the minimum calculation time interval so that other time variables are subordinate to Δt. Note that Δt decides the response speed of the entire control system because the convergence speed of the integrator of the expanded system shown in Fig. 4 depends on the Δt. Thus, the control response performance of the proposed method is strongly dependent on hardware performance, according to the above discussion. Based on the implementation results described later, the update time Δt was set to 500 μs, and the control horizon N was set to 5. The convergence coefficient ζ in (12) is proposed to

Control input

$I_{\text{com}}(t_n) = [I_{2\text{com}}, I_{3\text{com}}]^{\text{T}}$

$\Delta\phi_{(t_n)}$ $\int$ $\phi_{(t_n)}$

Plant

TAB Converter

$I(t_n) = [I_1(t_n), I_2(t_n), I_3(t_n)]^{\text{T}}$

$V(t_n) = [V_1(t_n), V_2(t_n), V_3(t_n)]^{\text{T}}$

C/GMRES

Current reference generator

$I_{m(0)}^{\text{ref}} = I_m(t_n)$

$I_{m(k+1)}^{\text{ref}} = \alpha I_{m(k)}^{\text{ref}} + (1-\alpha)(I_{\text{com}} + I_{\text{com\_offset}(k)})$

$I_m(t_n) = [I_{2m}(t_n), I_{3m}(t_n)]^{\text{T}}$

$I_m^{\text{ref}} = [I_{(0)}^{\text{ref}}, I_{(1)}^{\text{ref}}, \ldots, I_{(N-1)}^{\text{ref}}]^{\text{T}}$

$\Delta\phi(\tau) = [\Delta\phi_{(0)}(\tau), \Delta\phi_{(1)}(\tau), \ldots, \Delta\phi_{(N-1)}(\tau)]^{\text{T}}$

Sensor

Sensor and A/D converter

Control input tracking calculator

find $\Delta\phi(\tau)$ s. t. min $\left\|\dfrac{\partial H}{\partial \phi}\right\|$

solving $\dfrac{d}{d\tau} F(\Delta\phi(\tau), I_m(\tau), V_m(\tau), \tau)$

$= -\zeta F(\Delta\phi(\tau), I_m(\tau), V_m(\tau), \tau)$

$I_m(\tau) = [I_{m(0)}(\tau), \ldots, I_{m(N)}(\tau)]^{\text{T}}$

$\lambda(\tau) = [\lambda_{(1)}(\tau), \ldots, \lambda_{(N)}(\tau)]^{\text{T}}$

State and adjoint equation calculator

$I_{m(k+1)} = f(I_{m(k)}, \Delta\phi_{(k)}, V_{m(k)}) + I_{\text{offset}(k)}$

$\lambda_{(k)} = \dfrac{\partial H}{\partial I_m}(I_{m(k)}, \Delta\phi_{(k)}, \lambda_{(k+1)}, k)$

Digital LPF

$I_m(t_n) = \alpha I_m(t_{n-1}) + (1-\alpha)I(t_n)$

$V_m(t_n) = \alpha V_m(t_{n-1}) + (1-\alpha)V(t_n)$

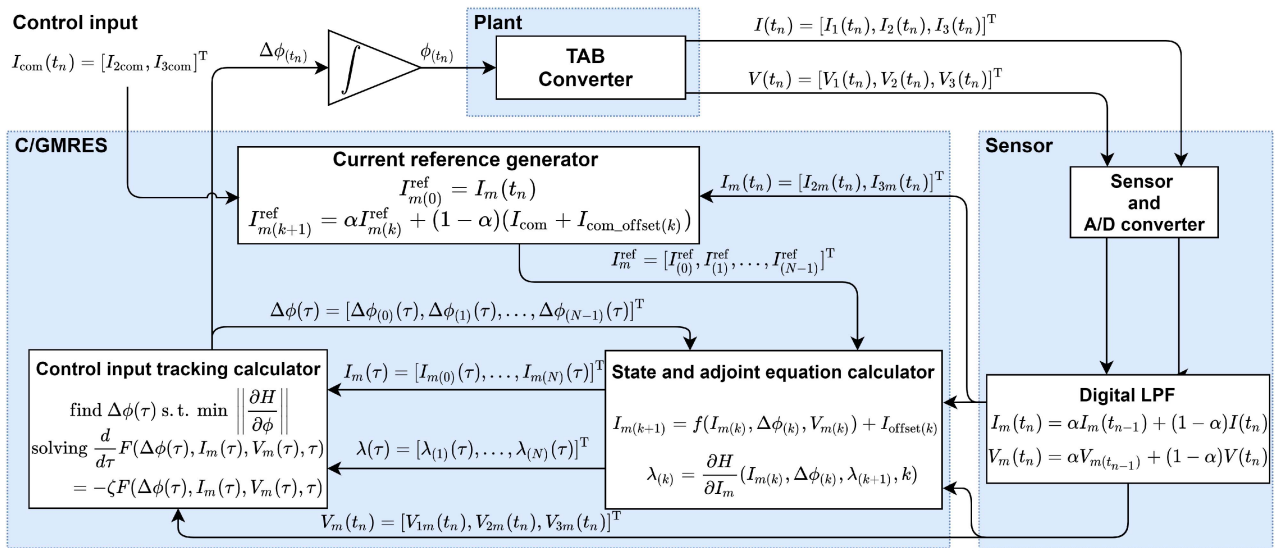$V_m(t_n) = [V_{1m}(t_n), V_{2m}(t_n), V_{3m}(t_n)]^{\text{T}}$

FIGURE 5. Block diagram of the proposed control system for TAB converter focusing on calculation procedures. (The calculation process of a control input tracking calculator is described in (5)∼(14). The calculation process of a current reference generator, and state adjoint equation calculator is described in (20)∼(27).)

TABLE 1. Basic Parameter Sets of the Proposed Control System.

Meaning	Symbol	Value
Control horizon	N	5
Update period of input vector	Δt	500 μs
Convergence coefficient	$\zeta = 1/\Delta t$	2000
Number of GMRES iterations	N_{G}	2
Number of C/GMRES iterations	N_{C}	4
Sampling period	$\Delta\tau = N_{\text{C}}\Delta t$	2 ms
Sampling frequency	$f_{\text{samp}} = 1/\Delta\tau$	500 Hz
Terminal cost weighting factor	r	0.01
Stage cost weighting factor	q	0.01
Input energy weighting factor	w	1
Command offset boundary	$I_{\text{com\_vic}}$	0.5 A
State variable offset boundary	I_{vic}	0.5 A

TABLE 2. Results of Parameter Tuning for Settling Time Adjustment

Control period		2 ms
Settling time		16 ms
Multi loop PI	P gain	0.05
	I gain	63
Decoupling control	P gain	0.35
	I gain	155
C/GMRES	r	0.035
	q	0.035
	w	1

be defined as the $1/\Delta t$ to ensure the stability of numerical calculations [26]. In addition, the number of GMRES iterations N_{G} was set to 2 since it is theoretically shown that N_{G} should be equal to or greater than the dimension of the matrix being calculated [30].

The other parameters were derived based on simulations. The number of iterations N_{C} was set to 4 based on the simulation described below. Consequently, the sampling period $\Delta\tau$ was derived to 2 ms, or sampling frequency f_{samp} was derived to 500 Hz. The weighting factors r, q, and w can be adjusted to match the desired response as parameters defining optimal operations. The operation of the control object is fundamentally determined based on the parameter ratios. In addition, it is known that the most robust condition is $w = 1$ from a disk margin theory [31]. Furthermore, basic ratios between input parameter w and state parameters r, q are derived from the open-loop gain of the control model (22). The open-loop gain

determinant $\det(G_{\text{open}})$ is expressed as the following equation at the operating point $\phi = 0$, where the determinant takes maximum value.

$$\det(G_{\text{open}}) = \begin{vmatrix} \partial I_{2m}/\partial\phi_2 & \partial I_{2m}/\partial\phi_3 \\ \partial I_{3m}/\partial\phi_2 & \partial I_{3m}/\partial\phi_3 \end{vmatrix} = \frac{12\,V}{\pi^3 f_{\text{sw}}3\,L} \quad (28)$$

From the terminal cost (26) and the stage cost (27), the fundamental ratios are expressed as the following equation.

$$r : q : w = \frac{1}{(\det(G_{\text{open}})^2)} : \frac{1}{(\det(G_{\text{open}})^2)} : 1 \quad (29)$$

To verify the validity of the control parameters and to observe the behavior of the variables that are difficult to observe in the experiment, simulations were conducted under the condition that step command $(I_{2\text{com}}, I_{3\text{com}}) = (0, 2)$ [A] is input to the TAB converter. The parameters of the circuit elements in the simulation are the same as in the following experiment, as shown in Table 3.

Fig. 6(a) shows the time variation of the norm of the error matrix $F(U(t), I(t), t)$. When the norm $|F|$ equals zero, the optimal condition is satisfied according to (10). The value of the norm $|F|$ at each simulation step decreases as the number

TABLE 3. Specifications of a Prototype TAB Converter

Main controller board		DE 10-Standard
Switching device		SCTH35N65G2V(600 V 45 A)
Switching frequency	f_{sw}	100 kHz
DC-bus voltage	$V_1 \sim V_3$	100 V
Transformer winding ratio		1:1:1
External inductance	L_1, L_2, L_3	10.02, 9.99, 10.15 μH
DC-bus capacitor		26.6 μF
Rated power of a inverter		1 kW
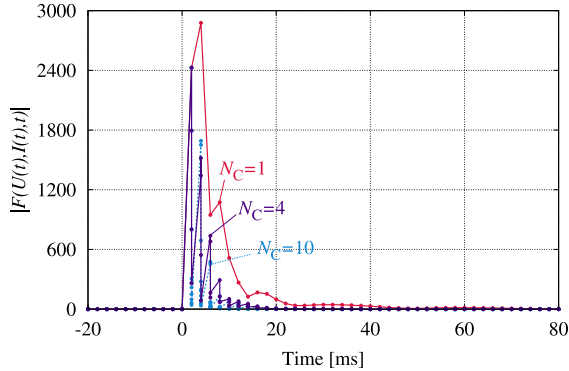
(a) Norm of error matrix F described in (10).
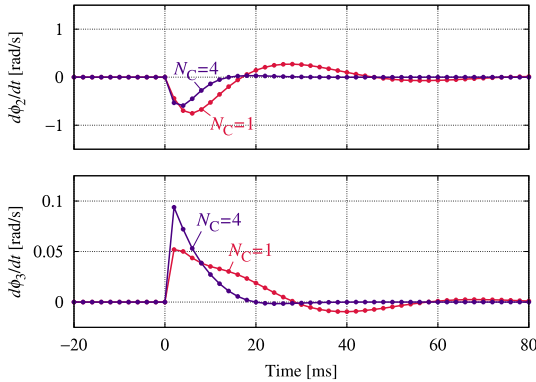
(b) Time derivative of phase-shift angles.
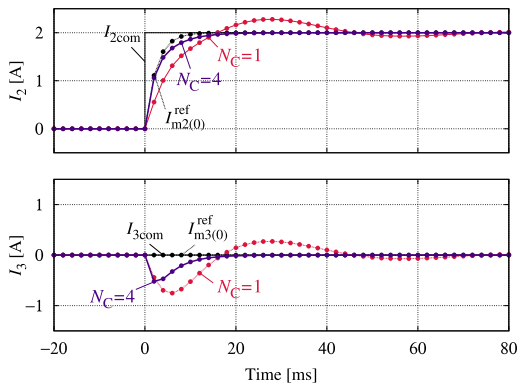
(c) Output currents.

FIGURE 6. Transition of internal parameters of the proposed controller under a step response from $(I_{2com}, I_{3com}) = (0, 0)$ to $(2, 0)$ [A] at 0 ms when optimization iteration number N_C changes.
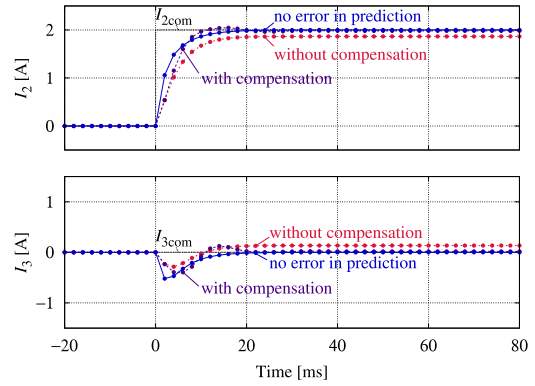
FIGURE 7. Current waveforms for step response comparison between with and without the compensator described in (25) when constant measurement error is imposed as $\Delta V_2 = \Delta V_3 = -20$ V against $V_2 = V_3 = 100$ V.

of C/GMRES iteration N_C increases from 1 to 4. In contrast, an increase in the number of iterations of N_C from 4 to 10 did not significantly affect the reduction of the norm. As N_C increases, the control response becomes slower because the finite calculation time is necessary for the actual system, unlike the simulation. Thus, $N_C = 4$ is a suitable parameter of iterations for the control system.

Figs. 6(b) and 6(c) show the transient response of $\frac{d\phi}{dt}$ and I when the step current command is input. The convergence to the command value is faster with $N_C = 4$ compared to $N_C = 1$, where the norm of F is close to zero at each simulation time.

Simulation results are shown at the last of this section to verify the validity of the compensator (25). The parameters discussed above were selected for the simulation. Fig. 7 shows the current transient response when the step command $(I_{2com}, I_{3com}) = (0, 2)$ [A] is input under the condition that the predictive calculation model has constant measurement errors in voltage V_2 and V_3, respectively. To make the difference clear between with and without the compensator, the error amounts $(\Delta V_2, \Delta V_3)$ [V] are exaggeratedly set to 20% of each voltage (V_2, V_3).

As a result, constant offsets are observed in the current responses without the compensator because MPC has no output feedback mechanism. On the contrary, it is confirmed that the offset caused by the measurement error can be reduced in the current responses with the compensator as shown in Fig. 7. This result suggests the validities of the offset compensator not only for measurement error but also for modeling error because an effect of measurement error in the process of prediction calculation is equivalent to an effect of modeling error (e.g., error of leakage inductance ΔL) in (20) and (21).

B. COMPARISON OF CONTROL METHODS

This section describes the simulation result of the comparison between control methods. Simple multi-loop PI control and the decoupling control methods established by previous research are compared to the proposed method. The decoupling
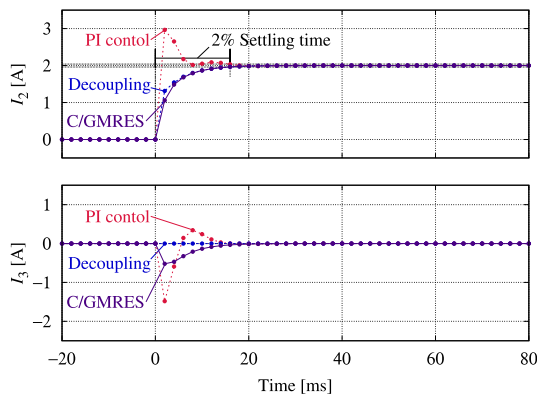
FIGURE 8. Current waveforms in step responses of each control method for a settling time adjustment when the current command changes from (0, 0) to (2, 0) [A] at 0 ms.
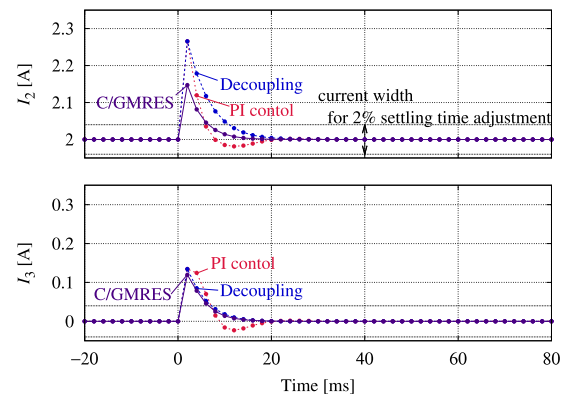

FIGURE 9. Current waveforms for comparison between each control method when primary-side voltage V_1 changes stepwise from 100 V to 120 V at 0 ms.

control method is an improved method of the multi-loop PI to solve the interference problem. The transient response of the proposed method is independent of the operating point because each current equally and asymptotically approaches the current command value according to the objective function (26) and (27). In contrast, the response of the decoupling compensator varies depending on the operating point. Thus, the comparison criteria are defined by the most advantageous conditions for the decoupling method. In other words, the control parameters of each control method are adjusted with the 2% settling time at the same operating point where the decoupler of the decoupling method is designed. In the previous research, it is clear that the decoupling effect enlarges when the current command value is set in the orthogonal direction (I_{2com}, 0) or (0, I_{3com}) [32]. In the following verifications, the transient responses are chosen where the effect of the decoupler is significant.

Fig. 8 shows the result of an adjustment of each control method. The 2%-settling time of each control method is adjusted with a step response when the current command (I_{2com}, I_{3com}) [A] is changed from (0, 0) to (2, 0) [A]. The parameters for the settling time adjustment are shown in Table 2. With these parameters, the transient response of multi-loop PI is accompanied by oscillations and overshoots, while the transient response of decoupling control is the ideal step response under the same settling time constraint. The proposed control method has intermediate performance between the two control methods:

- The transient responses of both the proposed and decoupling methods are similar for I_2, whose command value changes in step.
- The transient response of the proposed method deteriorates than decoupling control for I_3, whose command value is constant. These response characteristics are because the proposed method decreases the residual errors of the current references I_2 and I_3 simultaneously. In contrast, the residual error of the decoupling method does not occur at the operating point where the decoupler is designed.

Fig. 8 indicates that each current of the proposed method reaches the command value with a similar asymptotic waveform as results of optimization calculation with equal weighting factors for I_2 and I_3 in (26) and (27).

Fig. 9 shows transient responses when primary-side voltage changes from 100 V to 120 V with the adjustment parameters with constant current command (I_{2com}, I_{3com}) = (0, 2) [A]. It is confirmed that the deviation of the current from the command value due to voltage variation is suppressed compared with the multi-loop PI control and decoupling control. The result shows that the proposed method compensates for the current deviation by feed-forward control using the voltage values as opposed to the other methods that operate as feedback operations. On the other hand, The fact is also shown that the response speed of the proposed method is as slow as the response speed of the feedback control methods despite the feed-forward control. The cause of this response speed deterioration are attributed to the integrator used to configure the expansion system shown in Fig. 4 in the proposed method. Direct calculation of the input phase-shift variables without the integrator or direct reference to input variables by table modeling is expected to improve the response speed, which will be conducted in future work.

At the last of this section, a simulation result shows that the calculation process of the proposed method is more stable than the decoupling method. The design of the decoupler is difficult under the specific voltage conditions that the voltage of the phase reference (e.g., primary side in this paper) comes close to 0 because a determinant of a matrix, which the inverse matrix of the nominal model acting as a decoupler, diverges. On the contrary, the calculation of the proposed method is numerically stable in such conditions because the calculations of the nominal model are achieved by only substituting the forward equation (20) and (21).

Fig. 10 shows the waveforms when current commands are changed when the primary voltage changes to 0 V. Current command (I_{2com}, I_{3com}) is set to (1, 1) [A] at first, changed to (2, 2) [A] and (1, 1) [A] respectively when V_1 begins to decline and after V_1 becomes 0 V. The waveforms of Fig. 10 verify that
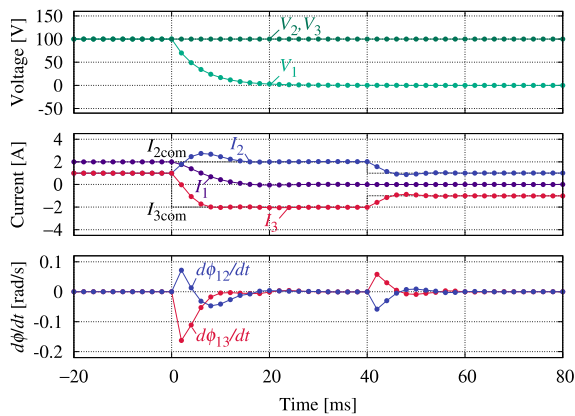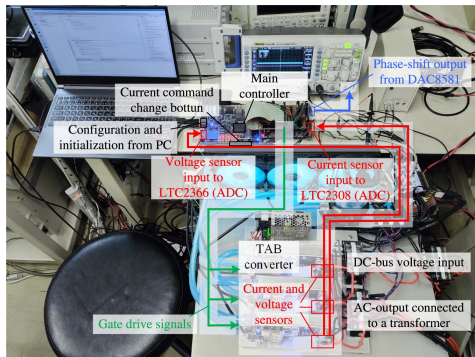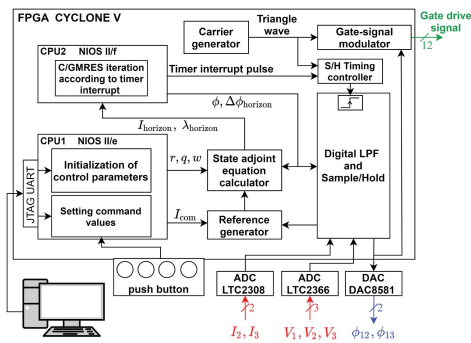
FIGURE 10. Waveforms when the phase reference voltage V_1 changes to 0 V. (The current command (I_{2com}, I_{3com}) is set to (1, 1) [A] at first, changes to (2, −2) [A] at 0 ms as V_1 begins to decline, and changes to (1, −1) A at 40 ms after V_1 reaches to 0 V.)

(a) Connection configuration of the proposed system.

(b) Configuration of the main controller.

**FIGURE 11.** Entire implementation diagrams.

the current control can be achieved when the voltage changes. This result supports that the proposed method is numerically stable against voltage changes.

IV. IMPLEMENTATION AND EXPERIMENTS

In this section, the implementation of the proposed method and experimental results are explained. The experiments were conducted using a prototype TAB converter consisting of the circuit elements shown in Table 3. The control system for the experiments was implemented using FPGA as the central
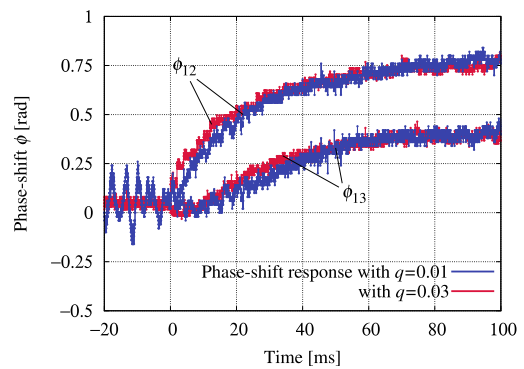
(a) Phase-shift response with different q.
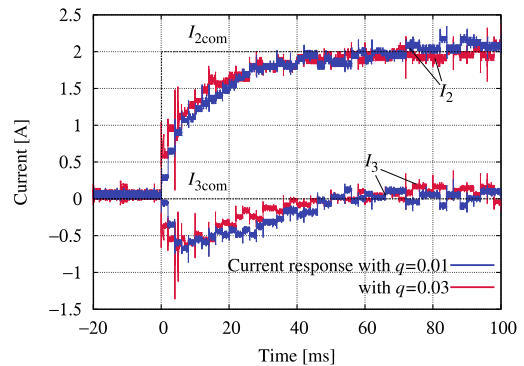
(b) Current response with different q.

FIGURE 12. Phase-shift and current response when step current command (I_{2com}, I_{3com}) = (2, 0) [A] is input with different weighting parameters q.
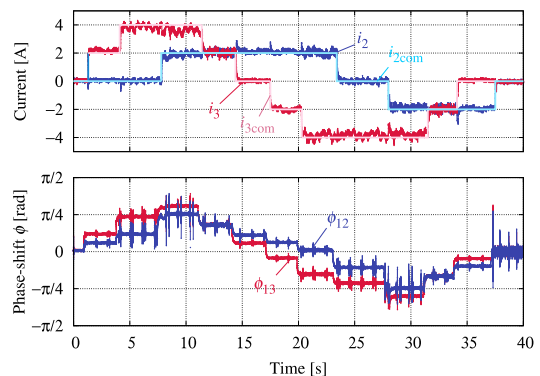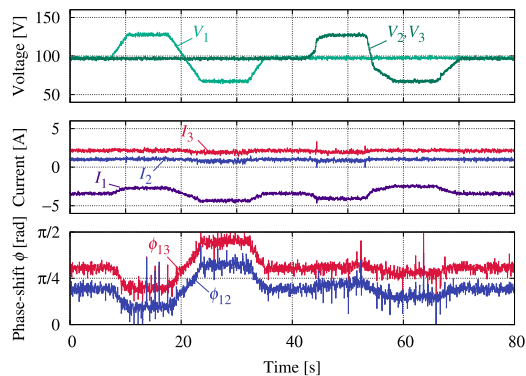

FIGURE 13. Current waveforms of current tracking control with multiple current command changes. (The current command is changed discretely as 0, ±2, ±4 A by push switches.)

controller. Fig. 11 shows the entire implementation diagram of the control system.

As shown in Fig. 11(a), the main controller received the voltage and current values from sensors equipped with the TAB converter through each A/D converter. The gate signals are calculated by two soft-core CPU and RTL circuits implemented into the FPGA according to the proposed method, as shown in Fig. 11(b). The phase-shift as the control input is outputted through a D/A converter to observe the transient response. In the FPGA, one CPU calculates command values decided by the computer or the push switch, and the other
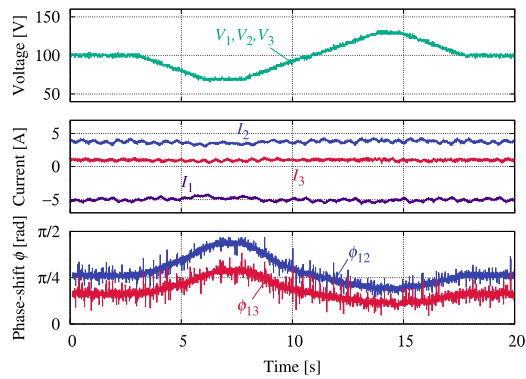
(a) All voltages change at the same time when the current command is fixed to $(I_{2com}, I_{3com}) = (4, 1)$ [A].

(b) Each voltage changes individually when the current command is fixed to $(I_{2com}, I_{3com}) = (1, 2)$ [A].

FIGURE 14. Experimental waveforms using the proposed current tracking control when the DC-bus voltages change.

calculates C/GMRES iteration calculations as the control input tracking calculator in Fig. 5. Other calculators in Fig. 5, including the current reference generator, the state and adjoint equation calculator, are implemented as RTL circuits.

Fig. 12 shows the change in step response when the weighting factor is changed. When the weighting factor q is changed from 0.01 to 0.03, the evaluation function term of the priority is given to follow the reference trajectory, resulting in a faster rise of the phase-shift as shown in Fig. 12(a). Consequently, the current converged faster to the command value as q was increased as shown in Fig. 12(b). These results confirm that the optimal transient response can be designed by changing the weighting factors.

Fig. 13 shows the measurement results of the current response over a long period to multiple command value changes. The current command value is updated to $(0, \pm 2, \pm 4)$ [A] by a push switch on the control board. The validity of the proposed control system for bidirectional power transmission is confirmed by the fact that all transient responses follow the bidirectional command value.

The approximately 2 ms periodic current ripples seen in Figs. 13 is attributed to the current-band compensation structure shown in (25). These current ripples are expected to

be reduced by applying adaptive control or observer system instead of band-type compensator.

Finally, the current response to voltage variations was verified by experiments. Fig. 14(a) shows the current response to voltage variations when the same power supply is connected to all DC-bus and the current command value is fixed at $(I_{2com}, I_{3com}) = (4, 1)$ [A]. The transmission power decreases as the voltage of the DC-bus decreases, and the phase-shift angles increase to maintain the current at the command value. Similarly, when the transmission power increases as the voltage increases, the current is maintained at the command value by decreasing phase-shift angles.

In addition, the response was measured when the voltage of each power supply was varied. A different voltage source from V_2 and V_3 was connected to V_1 as shown in Fig. 11; each voltage source was varied by 30% at different timing. Fig. 14(b) shows the current response to voltage variations the current command value is fixed at $(I_{2com}, I_{3com}) = (1, 2)$ [A]. As shown in Fig. 14(b), the primary-side current I_1 changes differently as shown in Fig. 14(a) due to the voltage ratio variations. In this case, it is confirmed that the current values are maintained at command values by appropriate phase-shift control.

V. CONCLUSION

A control system that can take voltage variation into the current tracking control model was constructed using the nonlinear model predictive control for the TAB converter. In the application process, a steady-state transmission power and a discrete state-space model based on a first-order time delay model suitable for the control method are proposed. The simulations clarified that the proposed method improves current response during voltage variation and the validity of parameter design. The experiments also described the feasibility of the proposed method, which can design transient responses. These results contribute to the development of the application of real-time long-horizon MPC to power converter control.

Also, several issues that need to be resolved were identified. At first, the integrator of the expanded system and its update time restrict the response speed of the entire control system. In particular, this problem is a direct cause of the lack of significant improvement in control performance relative to the cost of implementation. Next, the band-type compensator cannot solve the periodic ripple in steady-state, although it shows a certain performance to the offset characteristic of MPC. Our next target is to improve the proposed method by solving these problems and applying long-horizon MPC to a TAB converter under the condition that the voltages continuously change.

REFERENCES

[1] A. Imran et al., "Heuristic-based programable controller for efficient energy management under renewable energy sources and energy storage system in smart grid," *IEEE Access*, vol. 8, pp. 139587–139608, 2020. [Online]. Available: https://doi.org/10.1109/ACCESS.2020.301273510.1109/ACCESS.2020.3012735

[2] D. van der Meer, G. R. Chandra Mouli, G. Morales-España Mouli, L. R. Elizondo, and P. Bauer, "Energy management system with PV power forecast to optimally charge EVs at the workplace," *IEEE Trans. Ind. Informat.*, vol. 14, no. 1, pp. 311–320, Jan. 2018. [Online]. Available: https://doi.org/10.1109/TII.2016.263462410.1109/TII.2016.2634624

[3] A. Sangswang and M. Konghirun, "Optimal strategies in home energy management system integrating solar power, energy storage, and vehicle-to-grid for grid support and energy efficiency," *IEEE Trans. Ind. Appl.*, vol. 56, no. 5, pp. 5716–5728, Sep./Oct. 2020. [Online]. Available: https://doi.org/10.1109/TIA.2020.299165210.1109/TIA.2020.2991652

[4] H. N. de Melo, J. a. P. F. Trovão, P. G. Pereirinha, H. M. Jorge, and C. H. Antunes, "A controllable bidirectional battery charger for electric vehicles with vehicle-to-grid capability," *IEEE Trans. Veh. Technol.*, vol. 67, no. 1, pp. 114–123, Jan. 2018. [Online]. Available: https://doi.org/10.1109/TVT.2017.277418910.1109/TVT.2017.2774189

[5] Z. Ding, C. Yang, Z. Zhang, C. Wang, and S. Xie, "A novel soft-switching multiport bidirectional DC-DC converter for hybrid energy storage system," *IEEE Trans. Power Electron.*, vol. 29, no. 4, pp. 1595–1609, Apr. 2014. [Online]. Available: https://doi.org/10.1109/TPEL.2013.226459610.1109/TPEL.2013.2264596

[6] S. H. Hosseini, Z. Saadatizadeh, and P. C. Heris, "A new multiport non-isolated bidirectional DC/DC converter with zero voltage switching and free ripple input currents," in *Proc. 10th Int. Conf. Elect. Electron. Eng.* 2017, pp. 279–284.

[7] J. Zeng, W. Qiao, and L. Qu, "An isolated three-port bidirectional DC-DC converter for photovoltaic systems with energy storage," *IEEE Trans. Ind. Appl.*, vol. 51, no. 4, pp. 3493–3503, Jul./Aug. 2015. [Online]. Available: https://doi.org/10.1109/TIA.2015.239961310.1109/TIA.2015.2399613

[8] V.-L. Pham and K. Wada, "Normalization design of inductances in triple active bridge converter for household renewable energy system," *IEEJ J. Ind. Appl.*, vol. 9, no. 3, pp. 227–234, 2020. [Online]. Available: https://doi.org/10.1541/ieejjia.9.22710.1541/ieejjia.9.227

[9] Q. Mei, X. Zhen-lin, and W.-Y. Wu, "A novel multi-port dc-dc converter for hybrid renewable energy distributed generation systems connected to power grid," in *Proc. IEEE Int. Conf. Ind. Technol.*, 2008, pp. 1–5. [Online]. Available: https://doi.org/10.1109/ICIT.2008.460855510.1109/ICIT.2008.4608555

[10] Y. Kado, S. Okutani, K. Katagiri, and P.-Y. Huang, "Autonomous DC microgrid consisting of triple active bridge converters," in *Proc. IEEE 3rd Int. Conf. DC Microgrids*, 2019, pp. 1–5. [Online]. Available: https://doi.org/10.1109/ICDCM45535.2019.923281210.1109/ICDCM45535.2019.9232812

[11] C. Zhao, S. D. Round, and J. W. Kolar, "An isolated three-port bidirectional DC-DC converter with decoupled power flow management," *IEEE Trans. Power Electron.*, vol. 23, no. 5, pp. 2443–2453, Sep. 2008. [Online]. Available: https://doi.org/10.1109/TPEL.2008.200205610.1109/TPEL.2008.2002056

[12] X. Jun, Z. Xing, Z. Chong-Wei, and L. Sheng-yong, "A novel three-port bi-directional DC-DC converter," in *Proc. 2nd Int. Symp. Power Electron. Distrib. Gener. Syst.*, 2010, pp. 717–720. [Online]. Available: https://doi.org/10.1109/PEDG.2010.554578410.1109/PEDG.2010.5545784

[13] S. Okutani, A. Nishi, P.-Y. Huang, and Y. Kado, "Polar coordinate decoupling power flow control for triple active bridge converter," in *Proc. IEEE 3rd Int. Conf. DC Microgrids*, 2019, pp. 1–5. [Online]. Available: https://doi.org/10.1109/ICDCM45535.2019.923272010.1109/ICDCM45535.2019.9232720

[14] T. Ohno and N. Hoshi, "A new control method for triple-active bridge converter with feed forward control," in *Proc. Int. Power Electron. Conf.*, 2018, pp. 971–976. [Online]. Available: https://doi.org/10.23919/IPEC.2018.850778010.23919/IPEC.2018.8507780

[15] I. Biswas, D. Kastha, and P. Bajpai, "Small signal modeling and decoupled controller design for a triple active bridge multiport DC-DC converter," *IEEE Trans. Power Electron.*, vol. 36, no. 2, pp. 1856–1869, Feb. 2021. [Online]. Available: https://doi.org/10.1109/TPEL.2020.300678210.1109/TPEL.2020.3006782

[16] M. Neubert, A. Gorodnichev, J. Gottschlich, and R. W. De Doncker, "Performance analysis of a triple-active bridge converter for interconnection of future dc-grids," in *Proc. IEEE Energy Convers. Congr. Expo.*, 2016, pp. 1–8. [Online]. Available: https://doi.org/10.1109/ECCE.2016.785533710.1109/ECCE.2016.7855337

[17] T. Ohno and N. Hoshi, "Analysis of intermittent control for triple active bridge converter to suppress cross-current," in *Proc. IEEE 12th Energy Convers. Congr. Expo. Asia*, 2021, pp. 391–396. [Online]. Available: https://doi.org/10.1109/ECCE-Asia49820.2021.947901310.1109/ECCE-Asia49820.2021.9479013

[18] T. Geyer, *Model Predictive Control of High Power Converters and Industrial Drives*. Hoboken, NJ, USA: Wiley, 2017.

[19] P. Karamanakos, E. Liegmann, T. Geyer, and R. Kennel, "Model predictive control of power electronic systems: Methods, results, and challenges," *IEEE Open J. Ind. Appl.*, vol. 1, pp. 95–114, 2020. [Online]. Available: https://doi.org/10.1109/OJIA.2020.302018410.1109/OJIA.2020.3020184

[20] C. Jiang, J. Yang, S. Li, M. Zhou, and K. Yang, "Friction-compensation and extended state observer based model predictive control for pmsm servo systems," *IEEJ J. Ind. Appl.*, vol. 9, no. 4, pp. 351–357, 2020. [Online]. Available: https://doi.org/10.1541/ieejjia.9.35110.1541/ieejjia.9.351

[21] Y. Araki et al., "Harmonic current reduction control based on model predictive direct current control of ipmsm and input grid circuit," *IEEJ J. Ind. Appl.*, vol. 9, no. 1, pp. 17–26, 2020. [Online]. Available: https://doi.org/10.1541/ieejjia.9.1710.1541/ieejjia.9.17

[22] Z. Zhang, M. T. Larijani, W. Tian, X. Gao, J. Rodríguez, and R. Kennel, "Long-horizon predictive current control of modular-multilevel converter HVDC systems," in *Proc. 43rd Annu. Conf. IEEE Ind. Electron. Soc.*, 2017, pp. 4524–4530. [Online]. Available: https://doi.org/10.1109/IECON.2017.821677910.1109/IECON.2017.8216779

[23] E. Liegmann, P. Karamanakos, and R. Kennel, "Real-time implementation of long-horizon direct model predictive control on an embedded system," *IEEE Open J. Ind. Appl.*, vol. 3, pp. 1–12, 2022. [Online]. Available: https://doi.org/10.1109/OJIA.2021.313347710.1109/OJIA.2021.3133477

[24] M. Jeong, S. Fuchs, and J. Biela, "When FPGAs meet regionless explicit MPC: An implementation of long-horizon linear MPC for power electronic systems," in *Proc. 46th Annu. Conf. IEEE Ind. Electron. Soc.*, 2020, pp. 3085–3092. [Online]. Available: https://doi.org/10.1109/IECON43393.2020.925427710.1109/IECON43393.2020.9254277

[25] S. Fuchs and J. Biela, "Impact of the prediction error on the performance of model predictive controllers with long prediction horizons for modular multilevel converters - linear vs. nonlinear system models," in *Proc. 20th Eur. Conf. Power Electron. Appl.*, 2018, pp. 1–9.

[26] T. Ohtsuka, "A continuation/GMRES method for fast computation of nonlinear receding horizon control," *Automatica*, vol. 40, no. 4, pp. 563–574, 2004. [Online]. Available: https://www.sciencedirect.com/science/article/pii/S0005109803003637

[27] H. Nakada, P. Martin, A. Wijesinghe, H. S. A. Matsunaga, and H. Tominaga, "An application of C/GMRES model predictive control to a diesel engine air path system," *SICE J. Control, Meas., Syst. Integration*, vol. 54, no. 2, pp. 175–181, 2018. [Online]. Available: https://doi.org/10.9746/sicetr.54.17510.9746/sicetr.54.175

[28] M. Takekawa, J. Aoki, M. Nakaya, T. Ohtani, and T. Ohtsuka, "An application of nonlinear model predictive control using C/GMRES method to a ph neutralization process," in *Proc. SICE Annu. Conf.* 2010, pp. 1494–1496.

[29] T. O. J. Aoki and T. Ohtsuka, "A compensation method of offset caused by the nonlinear model predictive control using continuation/gmres method (in Japanese)," *Jpn. Joint Autom. Control Conf.*, vol. 51, pp. 910–915, 2008. [Online]. Available: https://doi.org/10.11511/jacc.51.0.181.010.11511/jacc.51.0.181.0

[30] Y. Saad and M. H. Schultz, "Gmres: A generalized minimal residual algorithm for solving nonsymmetric linear systems," *SIAM J. Sci. Stat. Comput.*, vol. 7, no. 3, pp. 856–869, 1983. [Online]. Available: https://doi.org/10.1109/CCA.2004.138760610.1109/CCA.2004.1387606

[31] P. Seiler, A. Packard, and P. Gahinet, "An introduction to disk margins," *IEEE Control Syst. Mag.*, vol. 40, no. 5, pp. 78–95, Oct. 2020. [Online]. Available: https://doi.org/10.1109/MCS.2020.300527710.1109/MCS.2020.3005277

[32] T. Ohno, K. Kakomura, and N. Hoshi, "Analysis of interference between each port in triple active bridge converter," *Elect. Eng. Jpn.*, vol. 207, no. 4, pp. 232–238, 2019. [Online]. Available: https://doi.org/10.1541/ieejias.139.23210.1541/ieejias.139.232

TAKANOBU OHNO (Member, IEEE) received the B.S., M.S., and Ph.D. degrees in power electronics from the Department of Electrical Engineering, Tokyo University of Science, Tokyo, Japan, in 2018, 2020, and 2022, respectively. He is currently an Research Fellow with the Tokyo University of Science. His research interests include topologies and control method of power converters, and renewable energy applications.

NOBUKAZU HOSHI (Senior Member, IEEE) received the B.S., M.S., and Ph.D. degrees in electrical engineering from the Department of Electrical Engineering, Yokohama National University, Yokohama, Japan. In 1997, he joined the Department of Electrical and Electronic Engineering, Ibaraki University, Hitachi, Japan, as a Research Associate and became an Assistant Professor in 2005. From 2008 to 2014, he was an Associate Professor and is currently a Professor with the Department of Electrical Engineering, Faculty of Science and Technology, Tokyo University of Science, Tokyo, Japan. His research interests include power electronics, motor control, electric vehicles, and hydrogen generation systems. He was the corecipient of IEEE IAS Committee Prize Paper Award in 1998 and 2010.